



ELSEVIER

Available online at www.sciencedirect.com

SCIENCE @ DIRECT®

Journal of volcanology
and geothermal research

Journal of Volcanology and Geothermal Research 132 (2004) 45–71

www.elsevier.com/locate/jvolgeores

Non-double-couple microearthquakes at Long Valley caldera, California, provide evidence for hydraulic fracturing

G.R. Foulger^{a,*}, B.R. Julian^a, D.P. Hill^a, A.M. Pitt^a, P.E. Malin^b,
E. Shalev^b

^a U.S. Geological Survey, 345 Middlefield Rd., MS 910, Menlo Park, CA 94025, USA

^b Division of Earth and Ocean Sciences, Nicholas School of the Environment, Box 90235, Duke University, Durham, NC 27708-0235, USA

Received 28 March 2003; accepted 2 December 2003

Abstract

Most of 26 small ($0.4 \leq M \leq 3.1$) microearthquakes at Long Valley caldera in mid-1997, analyzed using data from a dense temporary network of 69 digital three-component seismometers, have significantly non-double-couple focal mechanisms, inconsistent with simple shear faulting. We determined their mechanisms by inverting *P*- and *S*-wave polarities and amplitude ratios using linear-programming methods, and tracing rays through a three-dimensional Earth model derived using tomography. More than 80% of the mechanisms have positive (volume increase) isotropic components and most have compensated linear-vector dipole components with outward-directed major dipoles. The simplest interpretation of these mechanisms is combined shear and extensional faulting with a volume-compensating process, such as rapid flow of water, steam, or CO₂ into opening tensile cracks. Source orientations of earthquakes in the south moat suggest extensional faulting on ESE-striking subvertical planes, an orientation consistent with planes defined by earthquake hypocenters. The focal mechanisms show that clearly defined hypocentral planes in different locations result from different source processes. One such plane in the eastern south moat is consistent with extensional faulting, while one near Casa Diablo Hot Springs reflects an echelon right-lateral shear faulting. Source orientations at Mammoth Mountain vary systematically with location, indicating that the volcano influences the local stress field. Events in a 'spasmodic burst' at Mammoth Mountain have practically identical mechanisms that indicate nearly pure compensated tensile failure and high fluid mobility. Five earthquakes had mechanisms involving small volume decreases, but these may not be significant. No mechanisms have volumetric moment fractions larger than that of a force dipole, but the reason for this fact is unknown.

Published by Elsevier B.V.

Keywords: volcanic earthquakes; Long Valley caldera; seismic moment tensors; swarms; seismic sources

1. Introduction

The first convincing examples of 'non-double-couple' (non-DC) volcanic earthquakes, whose mechanisms are incompatible with simple shear faulting, were three moment magnitude (M_w)

* Corresponding author. On leave from Department of Geological Sciences, University of Durham, Science Laboratories, South Rd., Durham DH1 3LE, UK.

E-mail address: g.r.foulger@durham.ac.uk (G.R. Foulger).

5.5–6.2 earthquakes at Long Valley caldera, in eastern California, in 1978 and 1980. These were the M_w 5.5 Wheeler Crest earthquake of 4 October 1978 (Ekström and Dziewonski, 1983) and two of the four $M_w \sim 6$ earthquakes of 25 and 27 May 1980 (Barker and Langston, 1983; Julian, 1983; Julian and Sipkin, 1985). Since that time, non-DC microearthquakes have been identified at many other volcanic areas (Miller et al., 1998a), but the physical processes that cause them remain imperfectly understood, and it is not clear even that non-DC events of widely differing magnitudes are genetically similar. Julian (1983) and Julian and Sipkin (1985) suggested that the large 1978 and 1980 Long Valley earthquakes involved tensile failure caused by fluid pressure, but the seismic data available for these events could not resolve the volume changes that would accompany tensile faulting, so alternative explanations such as simultaneous slip on differently oriented shear faults have remained tenable. Recently, Dreger et al. (2000) fitted complete waveforms recorded on regional ‘broadband’ seismometers for six earthquakes of M_w 4.6–4.9 in December 1997, and showed that four of them have mechanisms with significant volume increases, and therefore must involve processes other than shear faulting.

Because of instrumental limitations, it has remained uncertain whether any of the thousands of microearthquakes that have occurred at Long Valley caldera since 1978 have non-DC mechanisms similar to those of the larger earthquakes. The permanent seismometer network in the area consists primarily of vertical-component sensors and uses analog telemetry and recording techniques with low dynamic range, so the only data bearing on focal mechanisms that they provide are P -wave first-motion polarities, which contain little information and are of little use for determining full moment-tensor source mechanisms (Julian et al., 1998).

To resolve questions about the mechanisms of microearthquakes at the caldera, the U.S. Geological Survey and Duke University installed and operated a temporary network of 65 three-component digital seismometers in the area from mid-May to late September 1997. During this pe-

riod, the caldera experienced a series of earthquake swarms, which intensified with time and were accompanied by accelerated ground deformation (Foulger et al., 1998). An unusually complete seismic data set was obtained for these swarms, covering earthquakes down to moment magnitudes less than 1.

In this paper, we describe results from analysis of this data set using methods based on arrival-time differences and amplitude ratios, which extract extra information from seismograms and are relatively insensitive to bias caused by wave-propagation anomalies. The derived focal mechanisms show that most of the earthquakes have volume increases, and therefore involve processes other than shear faulting. High-resolution relative earthquake locations further show that the failure geometry of some events is close to that expected for tensile faulting, but the mechanisms require an accompanying volume-compensating process, probably involving rapid fluid flow.

2. Long Valley caldera

The 17- by 30-km silicic Long Valley caldera is located at the northern end of Owens Valley, on the boundary between the Basin and Range province and the Sierra Nevada in eastern California (Fig. 1). The caldera floor lies roughly 2200 m above sea level, and contains a resurgent dome about 10 km in diameter, which rises about 300 m above the surrounding moat. The geology, geophysics and tectonic history of the area have been described in detail by many authors (e.g. Bailey et al., 1976; Hill et al., 1985; Rundle and Hill, 1988).

The caldera and the part of the Sierra Nevada immediately to the south have been seismically active since the M_w 5.5 Wheeler Crest earthquake of 4 October 1978, which occurred 10 km southeast of the caldera margin (Rundle and Hill, 1988). During this time, tens of thousands of earthquakes have occurred in the area, many of them during intense swarms. The four largest earthquakes to date, of $M_w > 6$, occurred on 25 and 27 May 1980, within and to the south of the caldera. Since then, seismic activity has been con-

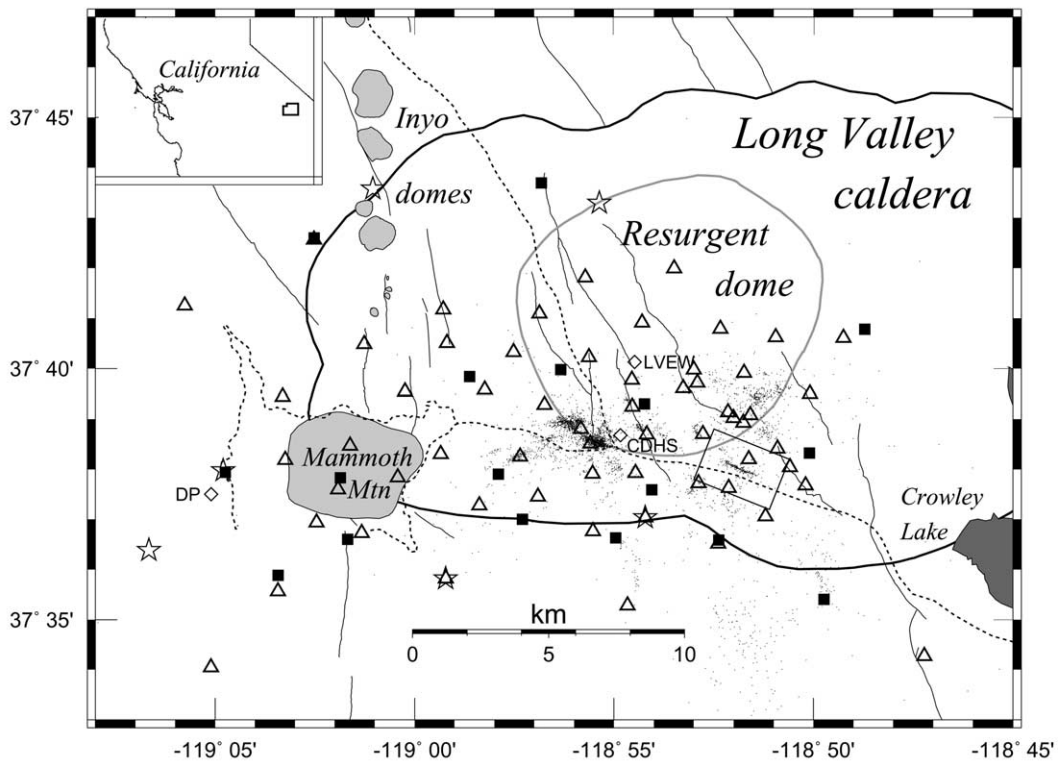


Fig. 1. Map of central and western Long Valley caldera and vicinity, showing permanent (squares) and temporary (triangles, stars) seismic stations operating in the summer of 1997 and epicenters (small dots) of 4472 microearthquakes that occurred from May through September. Stars: broad-band seismometers. The earthquake locations were computed by applying the Waldhauser and Ellsworth (2000) algorithm to 787232 *P*-phase arrival times measured from digital seismograms using the algorithm of R. Crosson (personal communication, 1993). Earthquakes within the oblique rectangle near the southeast margin of the resurgent dome clearly delineate an ESE–WNW-striking nearly vertical fault plane, and are shown in more detail in Fig. 7. Thick line: caldera boundary; thin lines: faults; gray line: resurgent dome; dashed lines: highways; CDHS: Casa Diablo Hot Springs; DP: Devil's Postpile; LVEW: the 3-km-deep Long Valley Exploration Well. Three short-period stations were located to the north, west, and south, outside the map boundary. Mammoth Mountain and the Inyo domes are shown in gray. Inset shows regional location of the main map.

tinuous and accompanied by intense earthquake swarms, rapid ground deformation, massive emissions of CO₂, and other evidence of volcanic unrest. Surges of resurgent-dome uplift and seismicity tend to coincide, most notably in 1989 and 1997–1998. Within the caldera, most earthquakes occur beneath the southern part of the resurgent dome, the south moat, and Mammoth Mountain. The most persistent seismic activity underlies the area around Casa Diablo Hot Springs in the south moat at depths between about 3 and 6 km b.s.l. Southeast of this region, activity is also intense on the ESE-striking south moat fault

(Denlinger et al., 1985), on which right-lateral strike-slip motion occurs.

A continuous background of earthquake activity occurs beneath Mammoth Mountain. In addition, an intense earthquake swarm occurred there in 1989, lasting about 6 months and accompanied by accelerated uplift of the resurgent dome. This swarm probably was accompanied by the injection of a dike about 13 cm thick in the depth range about –1 to 9 km b.s.l. (Hill et al., 1990; Langbein et al., 1993). At the same time, long-period earthquakes began occurring regularly at depths of 7–20 km b.s.l. southwest of Mammoth

Mountain (Pitt and Hill, 1994) (Fig. 1). Long-period earthquakes are deficient in energy above 5 Hz, occur only in volcanic areas, and probably are caused by unsteady fluid flow (Julian, 1994). Venting of up to 500 tons of CO₂ per day from faults dissecting Mammoth Mountain also began at the time of the 1989 swarm (Hill, 1996; Hill et al., 1990; Sorey et al., 1998, 1993), and subsequently has killed thousands of trees in several areas on the flanks of the mountain.

In the late spring of 1997, seismicity and the rate of inflation of the resurgent dome began to increase, and accelerated through the summer and fall, reaching their highest levels in late November. Activity decreased from early December onward, lasting into early 1998. Earthquakes as large as M_w 4.9 occurred in late November, and for the entire episode the Northern California Seismic Network (NCSN) of the U.S. Geological Survey located more than 20 000 events. At first, seismic activity was concentrated near Casa Diablo Hot Springs, but in November the south moat became active. During the whole episode, seismic activity beneath Mammoth Mountain continued at an approximately constant rate, while the rate of occurrence of deep long-period earthquakes beneath Devil's Postpile increased. The early part of the episode (July through September) was well recorded on a 69-station temporary seismic network that covered most of the seismically active area (Foulger et al., 1998) (Fig. 1). The data set acquired was used to perform high-resolution tomography of the southwest part of the caldera, the adjacent part of the Sierra Nevada, and Mammoth Mountain (Foulger et al., 2002). Comparison of the results with a tomographic image for the Mammoth Mountain area derived using data recorded in 1989 indicates possible changes in the ratio of the compressional- and shear-wave speeds (V_P/V_S) that suggest migration of CO₂ beneath the mountain between 1989 and 1997.

The 1997 seismic data are well suited for accurate focal-mechanism (moment tensor) determination because: (1) they cover the focal spheres of most local earthquakes densely; (2) they include all three components of motion; and (3) they are recorded with accurate timing, low noise, and

high dynamic range. In this paper we present moment tensors determined for 26 well-recorded earthquakes in the magnitude range 0.43–3.14. The number of earthquakes studied is limited only because the method we use is labor-intensive; hundreds of other earthquakes produced equally good data. The results show that many of the small earthquakes at Long Valley caldera have significant non-DC mechanisms, most having positive compensated linear-vector dipole (CLVD) components (Knopoff and Randall, 1970) and involving volume increases (i.e. $k > 0$ and $T < 0$; see Section 5.2). Such mechanisms suggest the involvement of fluid flow, and show that such processes are not limited to the large, non-DC earthquakes that have occurred in the area from time to time (e.g. Dreger et al., 2000; Julian and Sipkin, 1985).

3. Previous earthquake mechanism determinations for Long Valley caldera

The mechanisms derived for the three non-DC M_w 5.5–6.2 events of October 1978 and May 1980 were constrained to be deviatoric and are close to CLVDs with their largest principal moments extensional and oriented east-northeast. Julian (1983) and Julian and Sipkin (1985) suggested that they were caused by tensile failure associated with intrusion of fluids into NNW-striking vertical cracks and had intrusion volumes possibly as large as 0.07 km³. The active fluid was thought to be water or CO₂, although low-viscosity magma could not be ruled out. The seismic activity of 1980 migrated south-southwest from the resurgent dome, at depths of 5–8 km b.s.l. These depths are only slightly greater than that of the inferred center of inflation beneath the central resurgent dome, which is thought to lie about 3–6 km b.s.l. (Langbein, 1989; Langbein et al., 1995). These associations suggest a connection between the magmatic fluid flow that causes dome inflation and the shorter-term, seismogenic magmatism that may have caused the large earthquakes of 1980 (Julian, 1983).

The non-DC interpretations of Julian (1983) and Julian and Sipkin (1985) were controversial

at the time of publication because most seismologists attributed all earthquakes to shear faulting. Because the isotropic components of the 1978 and 1980 moment tensors could not be resolved with the data available, it remained possible that the non-DC mechanisms might be explained by simultaneous shear slip on multiple faults, for which the isotropic component vanishes. This hypothesis still requires, however, a physical explanation for the occurrence of several such earthquakes in an area within a short interval. Other suggested explanations of the observations included artifacts of the analysis methods used and biasing effects of complex structure on seismic-wave propagation. These hypotheses did not, however, provide reasonable explanations for a suite of seismic data that included long-period P and SH first motions and waveforms, amplitudes, phases and spectral amplitudes of long-period surface waves, and numerous short-period P -wave first motions (Julian and Sipkin, 1985). Furthermore, similar observations, including moment tensors with large volumetric components, have since been obtained from dense seismic networks at volcanic and geothermal areas in many other parts of the world (e.g. Arnott and Foulger, 1994; Console and Rosini, 1998; Foulger, 1988; Foulger and Long, 1984; Foulger et al., 1989; Hung and Forsyth, 1996; Kubas and Sipkin, 1987; Miller et al., 1998a; Saraò et al., 2001; Shimizu et al., 1988; Vavrycuk, 2002).

Although Long Valley caldera is intensively monitored for volcanic hazards, attempts to identify events with non-DC mechanisms among the thousands of smaller earthquakes since 1980 have been inconclusive. The NCSN includes about 20 stations within about 15 km of Casa Diablo Hot Springs, most of which have only single-component vertical sensors, use analog FM telemetry, which has limited dynamic range, and are not well calibrated. The only data relevant to focal mechanisms that such instrumentation can supply are P -wave polarities, and it is difficult to distinguish DC from non-DC mechanisms with P -wave polarities unless the mechanisms involve large volume changes and the focal-sphere coverage is unusually good. For many earthquakes, the NCSN polarity data are consistent with either DC or

pure-CLVD mechanisms, as well as a range of intermediate mechanisms and mechanisms having volume changes.

A suggestion that many of the small earthquakes at Long Valley caldera might have non-DC mechanisms is found in the preponderance of compressional (outward) P -wave polarities in NCSN data. About 56% of the $\sim 500\,000$ polarities measured during the 1990s, for example, are compressions, whereas for the coast ranges around San Francisco Bay the corresponding value is 49.3%. This bias cannot be the effect of random errors, but must be caused by some systematic effect. It is conceivable, however, that this effect involves source orientations and station distributions, and does not require non-DC mechanisms.

Savage and Cockerham (1984) determined fault-plane solutions for 19 earthquakes in a swarm in January 1993, whose hypocenters formed a dihedral distribution near Casa Diablo Hot Springs and along the south moat fault. They interpreted the solutions as indicating a mixture of right-lateral strike-slip and normal faulting beneath the Casa Diablo Hot Springs area, and pure right-lateral strike-slip faulting further east, on the south moat fault. Most of the T axes were approximately horizontal with trends that changed systematically from north to northeast at Casa Diablo Hot Springs to east to east-northeast on the south moat fault. The P axes ranged from approximately vertical to approximately horizontal, with trends ranging from north to west. These results suggest that the south moat fault may be a composite of more than one element with differing modes of failure, and that the direction of the least principal stress rotates clockwise moving eastward from Casa Diablo Hot Springs to the south moat.

Fault-plane solutions for a further 41 earthquakes in the south moat area from January 1989 through December 1991 yield a mixture of strike-slip, normal and normal-oblique faulting mechanisms, with P - and T -axis orientations similar to those inferred for the January 1983 earthquakes (Langbein et al., 1993). Almost all the earthquakes were in the Casa Diablo Hot Springs area, and so the variation in the orientations of

the T axes along the south moat fault could not be confirmed. The results imply highly variable faulting modes, and Langbein et al. (1993) concluded that the seismogenic volume beneath Casa Diablo Hot Springs is thoroughly brecciated, with slip occurring on variously oriented faults in close proximity to each other.

The variability of fault-plane solutions found in these studies might, however, be an artifact of constraining the mechanisms to be DCs and the incomplete coverage offered by real data sets. Sparse P -wave polarities from a non-DC earthquake are often compatible with a DC mechanism, though the DC nodal planes are usually not close to the true (non-planar) nodal surfaces. Fault-plane solutions (i.e. mechanisms constrained to be DC) for non-DC earthquakes tend to be sensitive to details in the data, and small changes in the true mechanism can produce large changes in the derived solution. Close examination of the observed polarity distributions of Langbein et al. (1993) suggests that they may suffer from this effect, because the data show less variation than the fault-plane solutions. Most of the dilatational arrivals lie in a high-angle, NW-trending band across the middle of the focal sphere, and the T axes are consistently oriented north to northeasterly. More consistency in the results might have been found had the data been of sufficient quality for derivation of full moment tensors so that the DC assumption would not have been necessary.

Recently Dreger et al. (2000) derived moment tensors for six M_w 4.6–4.9 earthquakes that occurred near Casa Diablo Hot Springs at the height of the swarm in November 1997, by inverting broadband waveforms, including P and S body waves and Love and Rayleigh surface waves, recorded on five three-component stations of the Berkeley Digital Seismic Network at regional distances. They found that four events had non-DC moment tensors with large CLVD and explosive volumetric components. Again, the mechanisms have high-angle, NW-trending dilatational fields across the middle of the focal spheres and T axes that are approximately horizontal and trend northeasterly. The source durations, of 2–2.5 s, are unusually large for earth-

quakes of these magnitudes. The focal depths lie in the range 4.5–7.5 km b.s.l., which is considerably shallower than the 11 km b.s.l. of the center of inflation beneath the Casa Diablo Hot Springs area inferred from deformation data (Langbein et al., 1995). Dreger et al. (2000) suggested that hydrothermal or magmatic fluid injection or pressurization of fluid-saturated faults caused the earthquakes. Such processes imply the upward migration of magma, water, steam, gas and/or heat and are thus consistent with a model of an active magma body underlying Casa Diablo Hot Springs at depths greater than about 8 km b.s.l. Moment tensors derived for two earthquakes in the Sierra Nevada south of Long Valley caldera using the same method are close to double couples, and are consistent with strike-slip and normal faulting.

4. Data and method

4.1. 1997 seismicity

We computed moment tensors for 26 earthquakes with NCSN duration magnitudes between 0.43 and 3.14 that occurred during the summer of 1997, in approximately the first half of the seismic episode described above. Earthquake swarm activity began just west of Casa Diablo Hot Springs on 7 July, about three weeks after inflation of the resurgent dome began to accelerate. During the summer the temporary network recorded more than 4000 locatable earthquakes, along with ~ 18 deep long-period events per week southwest of Mammoth Mountain. Most of the earthquakes were shallower than 8 km b.s.l. and clustered beneath Casa Diablo Hot Springs (Fig. 1). Earthquakes were also widely distributed throughout the southern part of the resurgent dome, the south moat, and Mammoth Mountain. Activity continued to increase after the network was decommissioned at the end of September, culminated with six earthquakes above magnitude 4.5 and thousands of smaller ones in late November (Barton et al., 1999), and then declined during December 1997 and January 1998.

We used data gathered on a dense temporary

69-station network that operated from 19 May through 30 September 1997 and covered an area of about 300 km², including the south moat, the southern part of the resurgent dome and Mammoth Mountain (Fig. 1). Foulger et al. (2002, 1998) and Stroujkova and Malin (2000) describe the experiment in detail. Six of the stations had three-component broadband sensors (Guralp models CMG3 and 40T) and the rest had three-component 2-Hz sensors (Mark Products model L-22). Data were recorded on 16- or 24-bit REFTEK data loggers with temperature-compensated quartz-crystal clocks synchronized to GPS or OMEGA radio time signals. All the broadband stations used 24-bit digitizers. Three stations were deployed at regional distances to the north, south and west of Mammoth Mountain in order to improve focal sphere coverage for the deep long-period earthquakes that occur southwest of Mammoth Mountain (Pitt and Hill, 1994). We supplemented the temporary-network data with data from approximately 17 NCSN stations, most of which had vertical 1-Hz sensors (Mark Products model L-4).

Fig. 1 shows the epicenters of 4472 earthquakes from the summer and early fall of 1997, computed by applying the method of Waldhauser and Ellsworth (2000) to data acquired by our temporary network. This method is often incorrectly called a ‘double-difference’ algorithm. Actually, it inverts a large set of single (one-station, two-earthquake) arrival-time differences, locating up to several thousand earthquakes simultaneously. It restricts its consideration to differences from nearby earthquake pairs, so that travel-time anomalies caused by unknown structural variations largely cancel out, and produces accurate relative locations that resolve well small-scale features of the earthquake distribution.

4.2. Polarity and amplitude measurement

We measured seismic-wave polarities and amplitudes by hand, using an interactive computer program. Fig. 2 shows example seismograms. We measured all *P* phases from vertical-component seismograms and *S* phases from horizontal seismograms that were numerically rotated to ra-

dial and transverse directions, except at stations close to the epicenter, where the radial and transverse directions become ill defined. In these cases we measured *S* phases on unrotated north- and east-component seismograms. The only data measured at single-component NCSN stations were *P*-phase arrival times and polarities. Before measuring amplitudes, we low-pass-filtered the seismograms using a three-pole Butterworth filter with a corner frequency of 5 Hz to remove higher frequencies, which are most subject to distortion by complicated crustal structure and anelastic attenuation. This filter has been found in previous studies to work well for data recorded on local networks of short-period sensors of the type used here (e.g. Miller et al., 1998b; Ross et al., 1999). Polarities measured on filtered and unfiltered traces nearly always agreed. The amplitudes measured were those of the first swing of each phase, rather than the largest (usually later) excursion, which is more likely to be contaminated by effects such as multipathing and near-surface mode conversion and reverberation.

4.3. Inversion method

We derived focal mechanisms (symmetric moment tensors) by fitting *P*-, *SH*- and *SV*-phase polarities and *P:SH*, *P:SV*, and *SH:SV* amplitude ratios using linear-programming methods (Julian, 1986; Julian and Foulger, 1996) to minimize the L_1 norm of the residuals between observed and theoretical values. Minimizing the L_1 norm is less sensitive than least-squares (L_2 -norm) fitting to large errors in a few observations (Claerbout and Muir, 1973). The use of amplitude ratios, rather than amplitudes, as data eliminates any dependence on instrument gain and greatly reduces errors caused by wave-propagation effects such as geometric spreading and near-receiver reverberation (Julian and Foulger, 1996). Such effects can severely distort the amplitudes of relatively high-frequency waves of the sort we use and preclude the use of simple amplitudes for determining focal mechanisms. Basing moment-tensor inversion on amplitude ratios instead of amplitudes reduces this distortion by an order of magnitude (see Section 4.5). Neither

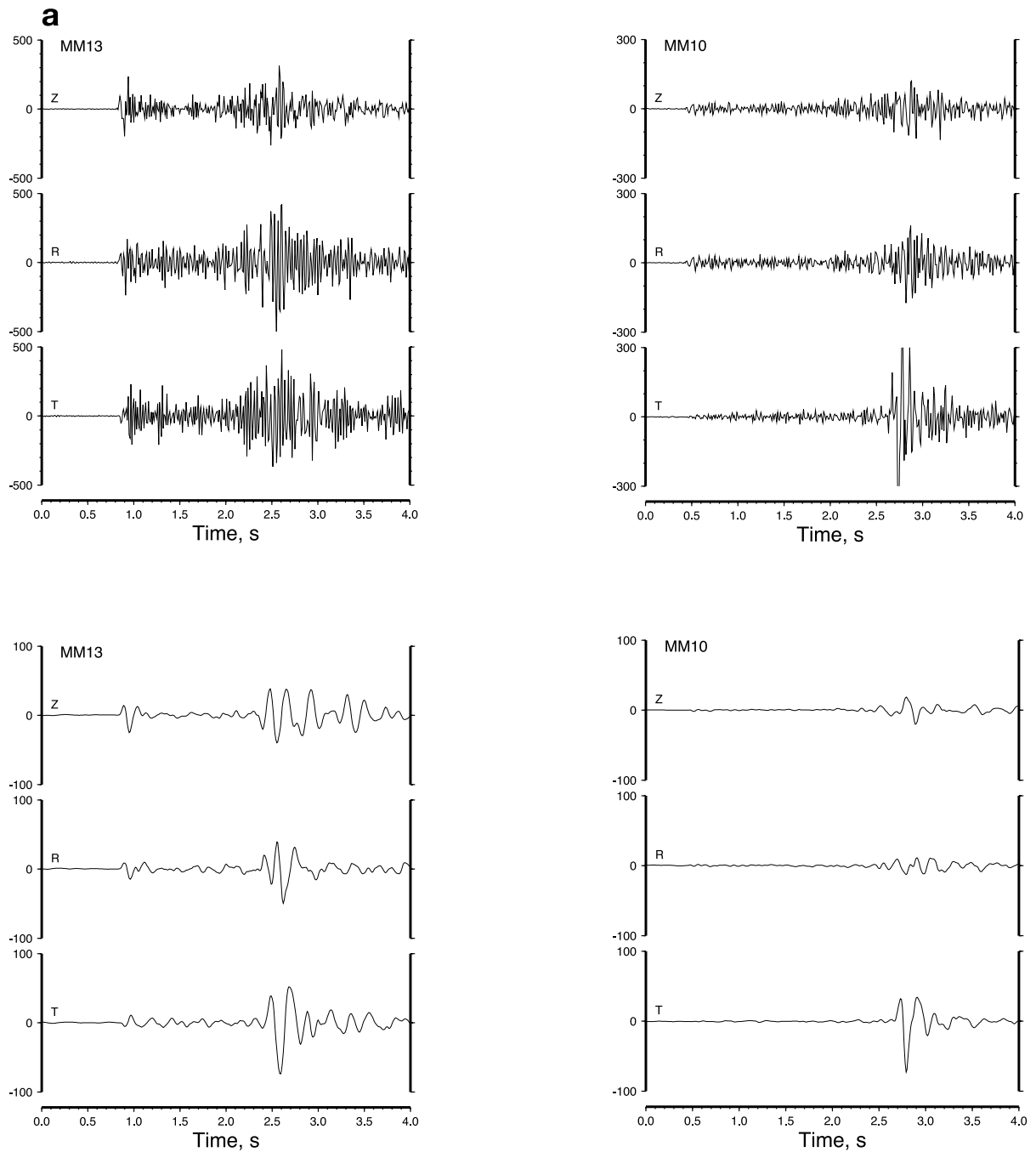


Fig. 2. Examples of representative seismograms. Top rows: rotated traces, bottom rows: the same, low-pass-filtered (Butterworth three-pole response with corner frequency of 5 Hz). (a) Event 18 (M_D 1.40) recorded at distances of 10.9 km (left) and 16.3 km (right). (b) Event 05 (M_D 3.01) recorded at distances of 26.9 km (left) and 4.84 km (right). Note the different time scales for panels a and b.

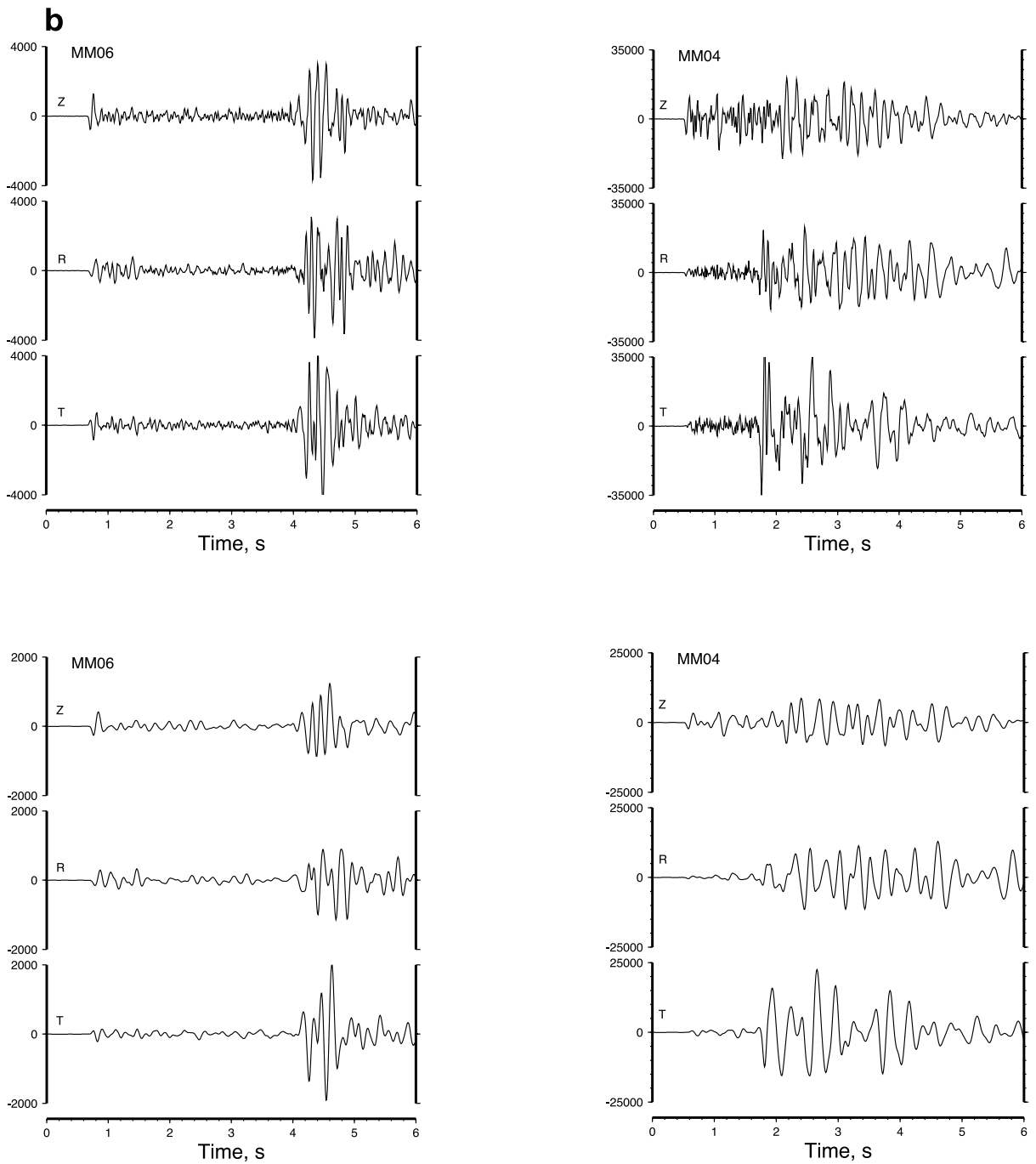


Fig. 2 (Continued).

wave polarities nor amplitude ratios contain any information about the scalar moment of an earthquake, so the moment tensors derived in this study are undetermined within an arbitrary scale factor.

Before determining moment tensors, we corrected the observed amplitudes for the effects of reflection at the free surface (modeled as a homogeneous half-space with a Poisson's ratio of 0.29, which is equivalent to $V_P/V_S=1.85$) and of attenuation caused by anelasticity and wave scattering. Because vertically polarized shear waves incident beyond the critical angle are severely distorted by interaction with the free surface, we used SV observations only when the theoretical off-nadir angles of incidence at the surface were less than 25° (within the 'shear-wave window'). P and SH waves account for almost all the useful data; SV waves contributed only a few polarity data and hardly any amplitude ratios. We mapped data onto focal spheres and computed incidence angles and azimuths by tracing rays through a three-dimensional model derived using local earthquake tomography. We also used hypocentral locations computed using the same model (Foulger et al., 2002) in this process. As in other studies of this kind (Foulger and Julian, 1993), we found that using a three-dimensional model instead of a one-dimensional model for locating events and mapping data onto the focal sphere has little effect on the focal mechanisms obtained.

4.4. Attenuation correction

Attenuation due to anelasticity and wave scattering affects compressional and shear waves differently, and multiplies an observed $P:S$ amplitude ratio by the factor:

$$\exp\left[-\frac{\omega}{2}\left(\frac{t_P}{Q_P}-\frac{t_S}{Q_S}\right)\right] = \exp\left[-\frac{\omega}{2}\frac{t_P}{Q_P}\left(1-\frac{Q_P}{Q_S}\frac{V_P}{V_S}\right)\right] \quad (1)$$

where ω is radian frequency, t is travel time, V is wave speed, and the 'figure of merit' (quality factor) Q is a characteristic of the propagation medium. Subscripts P and S indicate compressional and shear waves. We estimated the values of Q_P and Q_P/Q_S by inverting amplitude ratios from

well-recorded earthquakes using a range of values, and comparing the goodness of fit to the data achieved. The final values we used are $Q_P=120$ and $Q_P/Q_S=2.0$.

Prejean and Ellsworth (2001) recently studied attenuation at shallow depths beneath the resurgent dome of Long Valley caldera by comparing spectra of seismic waves recorded at the surface with those recorded at a depth of 2 km in the Long Valley Exploration Well. They found that Q_P lies in the range from 100 to 400 and $Q_P/Q_S \approx 0.50$. This Q_P/Q_S ratio differs significantly from the commonly assumed value of $9/4$, which corresponds to attenuation occurring only in shear (Anderson and Archambeau, 1964). For the values of Prejean and Ellsworth (2001), attenuation has little effect on $P:S$ amplitude ratios. From Eq. 1, with $f=5$ Hz, $t_P/Q_P \leq 0.03$ and $V_P/V_S=1.77$, amplitudes are reduced by 5% or less. We found that such a small correction gave significantly poorer fits to observed amplitude ratios than the values of $Q_P=120$ and $Q_P/Q_S=2.0$, and used these larger corrections in determining moment tensors.

4.5. Site effects

The motivation for using the ratio of the amplitudes of different phases at a station as a datum, rather than the amplitudes themselves, is to reduce the effects of wave propagation along different paths. This strategy is highly effective but not perfect; different seismic-wave modes propagate differently and some path and site effects can be expected to remain in the amplitude ratios. To estimate the magnitude of site effects, we computed theoretical seismograms for several hypothetical one-dimensional seismic wave-speed structures and filtered and measured wave amplitudes from them by applying the same procedures we used for real seismograms. Because we measure the amplitude of the first swing of each arrival, the largest effects are caused by structural variations near the surface, which produce converted phases and reverberations that arrive close enough to the time of the direct wave to affect the amplitude measurement.

We used the reflectivity method (Fuchs and

Müller, 1971) to compute theoretical seismograms for seven plane-layered models of structure within the caldera derived from the three-dimensional tomographic model of Foulger et al. (2002): an ‘unperturbed’ model in which the wave speeds at the surface are $V_P = 4$ and $V_S = 2.28$ km/s, and six models with surface layers 50, 100, and 200 m thick in which the wave speeds are reduced by factors of 2 and 4. For a source 7.5 km below the surface we measured the amplitudes of the P and SH waves at epicentral distances of 1, 2, 4, 8, and 16 km. These values are typical of the earthquakes and data used in this study.

The effects of the surface layers in these models are to perturb the $P:SH$ amplitude ratios by an average (median absolute value) amount of 4.5%, and at most by 22%. There is, moreover, no strong biasing effect; negative and positive perturbations are about equally common and the median perturbation is +2.6%. On the other hand, the effect on the raw amplitudes is strong and systematic. The different surficial layers used in this test increase the P amplitudes by 22.5% to 79.4% (median: 45.8%) and SH amplitudes by 20.6% to 67.1% (median: 35.9%). Thus the strategy of using amplitude ratios rather than amplitudes reduces errors caused by near-surface site effects by an order of magnitude, to a level that is negligible compared to other sources of error, such as signal-generated noise contaminating the SH arrival (see Fig. 2).

4.6. Resolving power

An estimate of the uniqueness of our derived focal mechanisms can be obtained by comparison with a similar study of earthquakes at the Hengill-Grensðalur area in southwest Iceland by Miller (1996), who assessed the quality of his solutions by inverting randomly chosen subsets of the data for a single earthquake. For the best solutions, he estimated the probable errors in the source-type parameters to be about 0.1 for k and 0.2 for T (see Section 5.2, Eqs. 2 and 3). The 1997 station network at Long Valley caldera was much denser (69 stations versus 30, and in a smaller area), so the errors in our study probably are smaller.

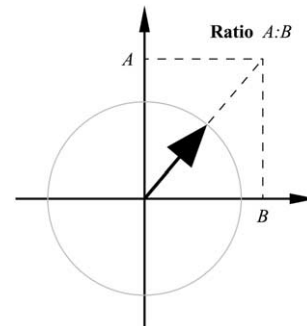


Fig. 3. Graphical convention used to represent amplitude ratios in Fig. 4. An arrow of unit length whose slope is A/B represents the ratio $A:B$. Each quadrant corresponds to a unique combination of the signs of A and B . This representation includes information about the signs of the amplitudes A and B , and does not cause strong visual distortion when A or B is small.

4.7. Example solutions

Figs. 3 and 4 show our data-display convention and examples of the fits to the data for five earthquakes. Numerical data for these earthquakes are given in Tables 1 and 2. Earthquake 5 (Fig. 4a) is located near Casa Diablo Hot Springs and has a large data set with numerous P and SH polarities and amplitude observations covering the upper focal hemisphere well. The derived focal mechanism fits the data well. Fig. 4b compares the same data with the theoretical predictions for the DC component of our derived mechanism for this earthquake, computed by the method of Knopoff and Randall (1970). The non-DC mechanism fits both the P -wave polarities and the $P:SH$ amplitude ratios significantly better than the DC does. Earthquake 18 (Fig. 4c) is located south of the south moat fault. It is somewhat southerly in our network and consequently the data cover the focal sphere less well than for centrally located earthquakes. Nevertheless, the data coverage is extraordinarily good compared with most focal mechanisms, and our use of a variety of data types enables us to resolve the mechanism well. Earthquake 19 (Fig. 4d) is located beneath Mammoth Mountain and is an example of one of the few earthquakes we studied that have small implosive components. Earthquake 20 (Fig. 4e) is

Table 1
Earthquakes analyzed

Event	Date UTC	Time UTC	Latitude	Longitude	Depth km b.s.l.	M_D^a
1	25 Jun	04:05:47.516	37:38.640	-118:54.949	2.920	1.10
2	30 Jun	08:21:58.313	37:38.128	-118:58.263	4.984	2.02
3	01 Jul	09:26:29.243	37:38.893	-118:51.427	5.120	0.77
4	07 Jul	03:58:36.033	37:40.486	-118:57.189	1.525	1.05
5	08 Jul	21:35:39.944	37:38.977	-118:55.903	4.738	3.01
6	10 Jul	07:14:19.348	37:39.028	-118:56.164	4.574	3.14
7	11 Jul	08:46:33.792	37:38.631	-118:55.670	4.595	1.35
8	11 Jul	08:55:18.899	37:38.523	-118:55.615	4.236	0.84
9	17 Jul	14:06:10.462	37:38.098	-118:52.067	3.030	1.95
10	18 Jul	01:37:00.092	37:38.176	-118:52.142	3.165	2.48
11	18 Jul	10:26:02.121	37:38.155	-118:52.263	3.304	1.82
12	12 Aug	08:25:24.077	37:38.417	-118:58.135	4.041	1.07
13	23 Aug	08:10:03.521	37:37.845	-118:57.479	5.555	1.56
14	29 Aug	18:08:31.669	37:38.269	-118:57.476	3.424	0.43
15	29 Aug	18:39:36.796	37:38.287	-118:57.497	3.726	1.05
16	29 Aug	20:12:15.447	37:38.074	-118:57.910	4.336	0.77
17	30 Aug	05:30:23.438	37:38.236	-118:57.459	3.837	0.95
18	30 Aug	19:10:51.156	37:37.102	-118:56.015	1.586	1.40
19	04 Sep	06:14:41.287	37:38.325	-119:01.672	2.129	1.19
20	04 Sep	14:58:12.040	37:37.543	-119:02.166	1.950	1.16
21	04 Sep	14:58:45.688	37:37.400	-119:01.937	2.756	–
22	06 Sep	19:29:35.808	37:37.282	-119:01.373	2.060	–
23	06 Sep	19:29:52.559	37:37.322	-119:01.439	1.984	1.42
24	07 Sep	01:20:33.366	37:37.598	-119:02.618	0.000	1.55
25	07 Sep	11:43:21.178	37:37.341	-119:01.353	1.807	1.17
26	07 Sep	15:44:38.577	37:37.417	-119:01.450	2.134	0.78

^a M_D : duration magnitude from NCSN catalog.

also located beneath Mammoth Mountain. It occurred during a spasmodic burst and its mechanism has a large explosive component. Earthquake 11 (Fig. 4f) is located southeast of the resurgent dome, at the east end of the south moat. It is one of many earthquakes whose hypocenters outline an ESE-striking vertical plane, and we discuss it in more detail below.

The examples in Fig. 4 illustrate the importance of using amplitude ratios along with polarities in

determining focal mechanisms. Source types have second-order effects on seismic data, and are more difficult to determine than source orientations (fault-plane solutions). Particularly when the volumetric component is small, wave polarities alone are rarely sufficient to resolve source types well. Polarity data usually are consistent with a range of possible solutions and a DC is often among them (Julian and Foulger, 1996). If polarity data alone were used, a DC mechanism could,

Fig. 4. Examples of fit to data for six focal mechanism solutions. Data are plotted on upper focal hemispheres, shown in equal-area projection. Top row: P -, SH - and SV -wave polarities. Filled symbols indicate motion outward for P , counter-clockwise around the epicenter for SH , and away from the epicenter for SV . Open symbols indicate the opposite polarities. Circles: upper-hemisphere data; squares: lower-hemisphere data, plotted at antipodal points. Lines: theoretical nodal curves for derived mechanism. Bottom row: $P:SH$ and $SH:SV$ amplitude ratios displayed as illustrated in Fig. 3. Black arrows: observed ratios; outlined arrows: theoretical ratios for derived mechanism. $P:SH$ ratios are multiplied by $(V_P/V_S)^3$ to correct for the systematic difference in average P - and S -wave amplitudes. Dates and times of earthquakes are shown at the upper left. (a) Earthquake 5. (b) Same, for DC mechanism. (c) Earthquake 18. (d) Earthquake 19. (e) Earthquake 20. (f) Earthquake 11. See Tables 1 and 2 for numerical data corresponding to these earthquakes.

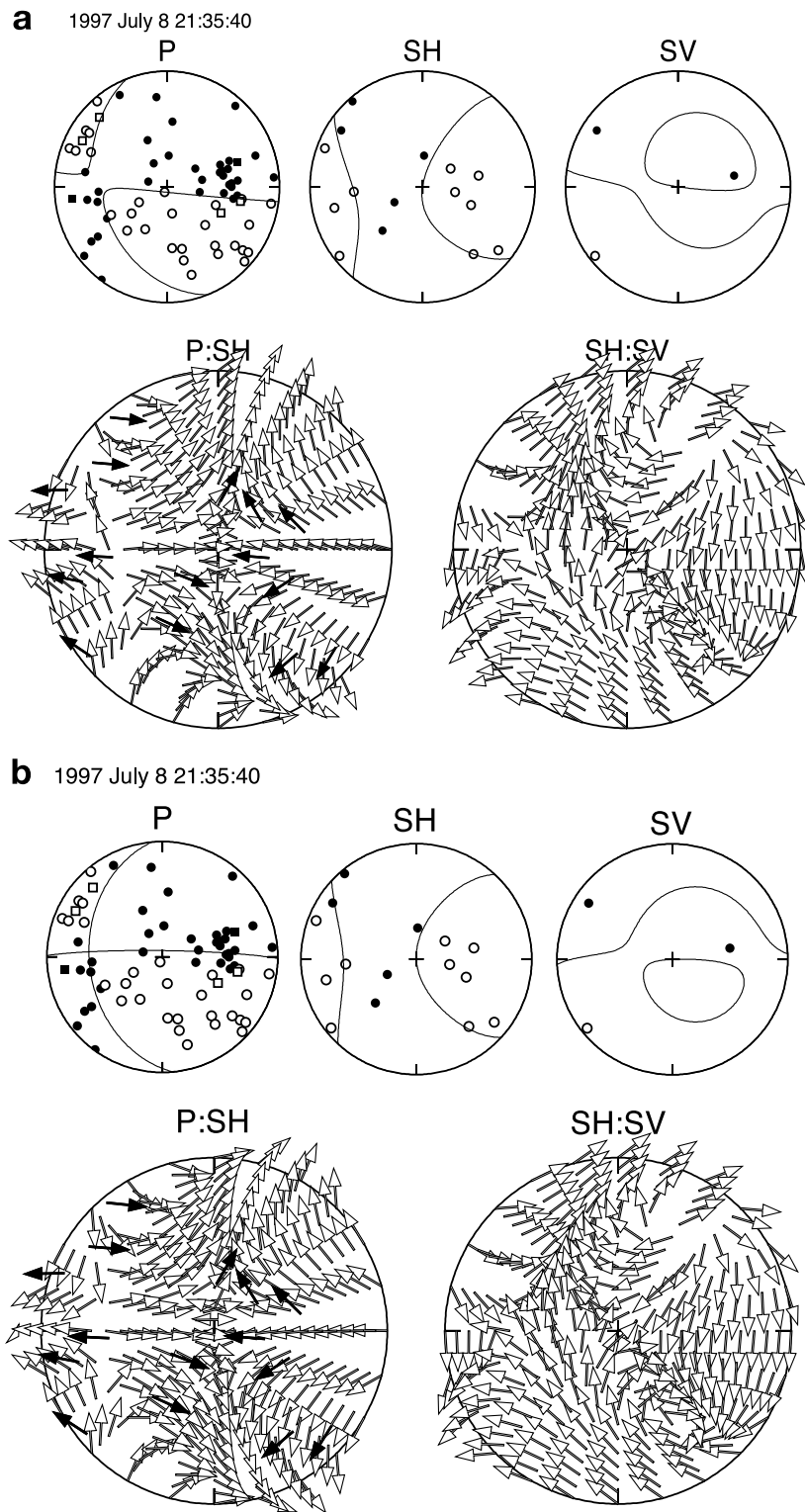


Fig. 4.

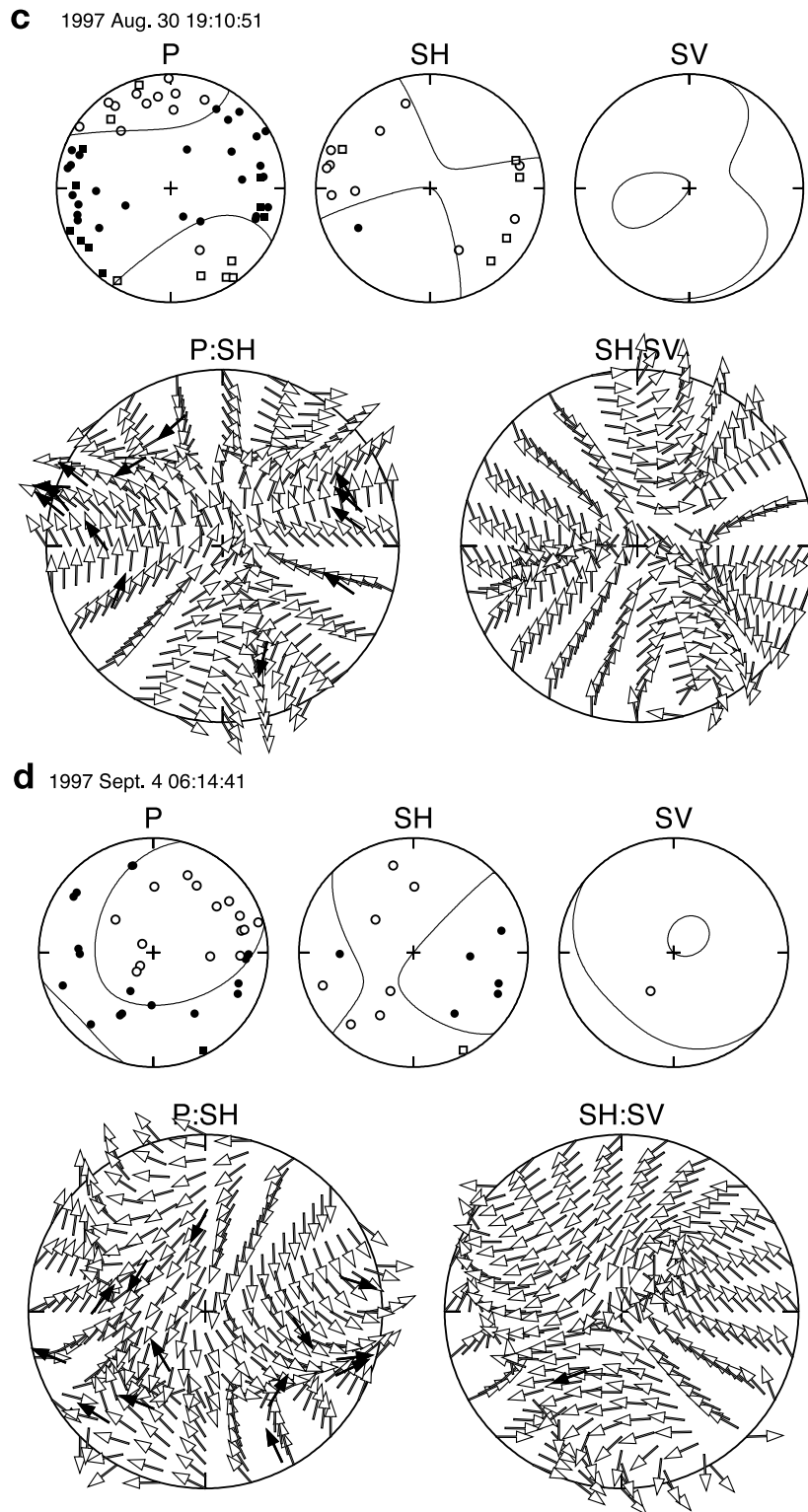
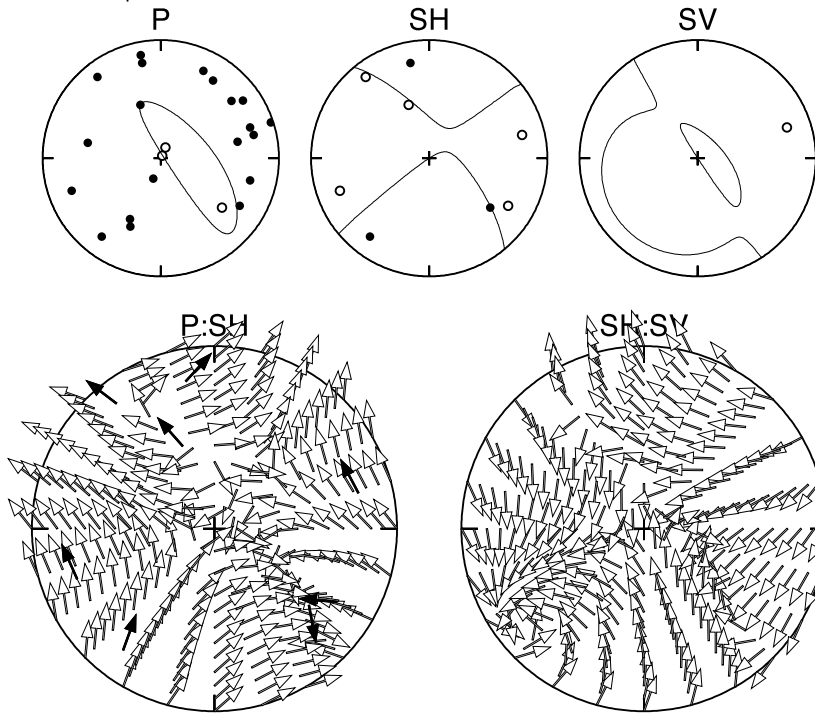


Fig. 4 (Continued).

e 1997 Sept. 4 14:58:12



f 1997 July 18 10:26:02

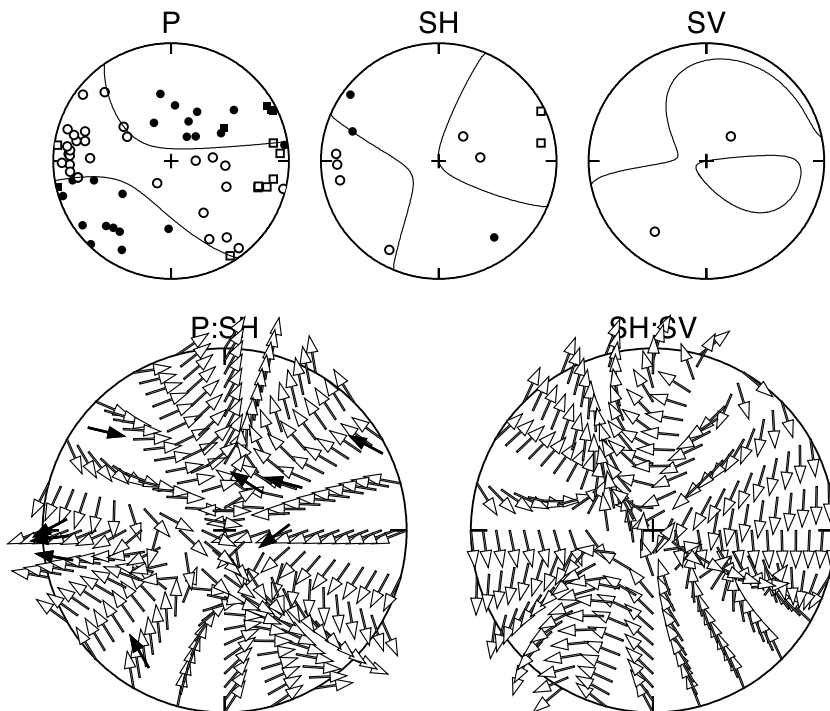


Fig. 4 (Continued).

Table 2
Focal mechanisms

Event	M_{xx}	M_{xy}	M_{yy}	M_{xz}	M_{yz}	M_{zz}	k	T	M	t deg.	p deg.
1	1.543	0.786	0.336	-2.441	0.353	0.961	0.25	-0.23	3.75	188	40
									0.63	79	21
									-1.54	328	42
2	2.913	0.257	0.358	-1.989	0.594	-1.048	0.20	-0.14	3.74	180	23
									0.53	84	14
									-2.05	325	63
3	2.136	1.833	-1.208	0.310	1.173	-0.024	0.10	-0.09	3.14	26	14
									0.18	146	63
									-2.41	290	23
4	0.131	0.803	1.627	1.412	1.063	-1.687	0.01	0.01	2.57	60	21
									0.04	323	16
									-2.54	199	63
5	1.202	1.644	0.405	-2.106	-0.309	0.274	0.17	-0.38	3.60	210	31
									0.06	94	37
									-1.78	328	38
6	-0.805	2.203	-0.797	-1.322	-0.086	1.176	-0.04	0.36	2.36	216	43
									0.41	59	44
									-3.19	318	12
7	4.725	-1.020	-2.364	-0.166	-0.176	-0.184	0.15	-0.43	4.87	172	2
									-0.17	280	85
									-2.52	82	5
8	1.592	1.015	-1.152	0.457	1.692	-0.927	-0.06	0.14	2.28	26	20
									0.01	136	42
									-2.78	278	41
9	1.248	1.124	0.471	-1.922	-0.503	-1.185	0.06	-0.23	2.92	210	25
									-0.14	113	15
									-2.25	355	60
10	1.507	2.553	0.385	-0.832	-0.483	-0.372	0.13	-0.66	3.78	218	13
									-0.57	69	75
									-1.69	310	7
11	3.129	1.990	-0.721	-0.584	0.200	-0.603	0.15	-0.64	4.02	203	6
									-0.49	98	68
									-1.72	295	21
12	-0.543	1.342	0.767	-1.525	-0.755	1.446	0.18	-0.20	3.06	227	45
									0.31	83	39
									-1.70	337	19
13	2.813	1.650	-1.043	0.792	0.487	0.288	0.19	-0.42	3.67	21	15
									0.06	179	74
									-1.67	289	6
14	3.795	1.720	-1.159	0.059	-0.272	-0.944	0.13	-0.75	4.33	197	0
									-0.85	288	72
									-1.79	107	18
15	3.606	1.454	-1.113	-0.527	0.464	-0.390	0.17	-0.52	4.05	195	5
									-0.17	94	66
									-1.78	287	23
16	2.772	1.468	-1.154	0.668	0.531	-0.739	0.09	-0.70	3.42	19	11
									-0.80	138	68
									-1.74	285	19
17	-0.956	1.217	1.079	-0.846	-1.325	1.190	0.15	-0.45	3.00	243	41
									-0.14	75	48
									-1.55	338	6

Table 2 (Continued).

Event	M_{xx}	M_{xy}	M_{yy}	M_{xz}	M_{yz}	M_{zz}	k	T	M	t deg.	p deg.
18	−2.132	1.223	1.878	−0.234	0.794	1.487	0.12	0.47	2.66	77	32
									1.10	243	57
									−2.52	343	6
19	0.589	−1.215	0.579	1.166	0.945	−2.180	−0.11	0.44	1.81	317	3
									0.27	49	31
									−3.09	222	59
20	1.467	1.676	2.112	0.588	0.912	0.072	0.32	−0.84	3.81	51	16
									0.12	146	18
									−0.28	281	66
21	2.421	2.432	1.974	−0.099	0.192	−0.158	0.30	−0.87	4.64	42	1
									0.01	133	51
									−0.41	312	39
22	1.639	−0.899	0.821	−1.447	1.095	−0.659	0.19	−0.28	3.09	146	26
									0.25	54	3
									−1.54	318	64
23	1.951	−1.322	1.518	−0.703	0.434	−1.612	0.19	−0.17	−1.76	339	80
									0.40	231	3
									3.21	140	10
24	−0.592	0.982	−1.052	−1.829	0.843	1.046	−0.07	0.09	2.24	173	58
									−0.09	56	16
									−2.75	317	27
25	1.613	−0.451	1.004	−1.253	0.523	−2.929	−0.03	0.55	2.21	153	15
									0.77	244	1
									−3.29	339	75
26	1.032	0.867	1.844	−0.534	1.601	−1.120	0.18	0.35	2.76	69	18
									1.05	167	22
									−2.05	303	60

Seismic moments in arbitrary units. x , y , z axes directed north, east, and down. k , T : source-type parameters (Eqs. 3 and 2). M : Principal moment (arbitrary units). t , p : Trend and plunge of principal axis.

for example, be fit to the data of event 18 (Fig. 4b) with few violations, and such analyses are common in seismology. The addition of amplitude-ratio data, however, more tightly constrains the mechanisms and shows that many of them have significant non-DC components.

5. Results

Table 1 gives hypocentral coordinates and magnitudes for the 26 earthquakes analyzed, and Table 2 gives the derived focal mechanisms, in the form of moment-tensor components, source-type parameters (see below), principal moments, and principal-axis orientations. The moment tensors are normalized arbitrarily, so only the relative values of the moment-tensor components and principal moments are significant. Fig. 5 shows

the geographical distribution of the mechanisms and previously published mechanisms for earthquakes from 1980 and 1997 (Dreger et al., 2000; Julian and Sipkin, 1985).

5.1. Source orientations

One of the most consistent characteristics of the earthquake mechanisms at Long Valley caldera in the 1980s and 1990s has been the orientation of their T axes, which are subhorizontal and trend approximately northeast, in the same direction as persistent horizontal extension during the same time period (Langbein et al., 1993). The earthquakes in the caldera that we analyzed are consistent with this generalization, although the T -axis trends average approximately north-northeast. These trends resemble the results of Savage and Cockerham (1984), who found a more north-

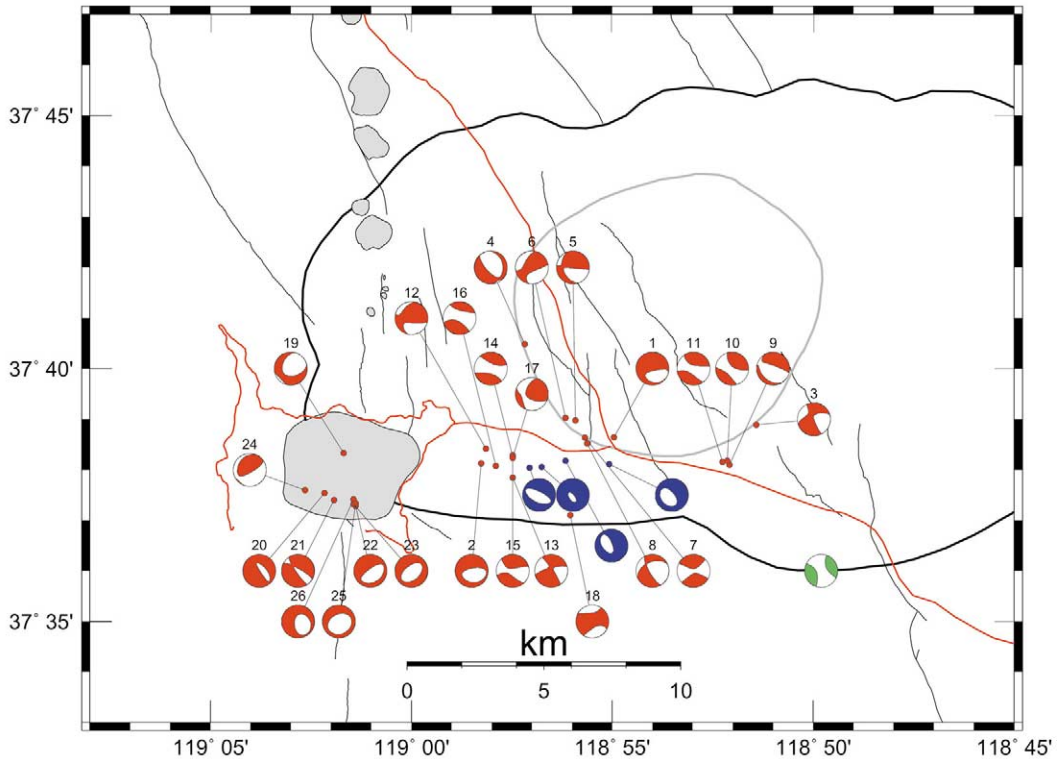


Fig. 5. Earthquake focal mechanisms, plotted on base map of Fig. 1. Each circle shows the theoretical far-field P -wave polarity pattern on an equal-area projection of the upper focal hemisphere, with the compressional field filled. Red: mechanisms reported in this paper; blue: mechanisms of M 4.5–4.9 earthquakes of November 1997, as reported by Dreger et al. (2000); green: mechanism of the 16:44 event of 25 May 1980, as reported by Julian and Sipkin (1985), which was constrained to be deviatoric. The other three well-constrained earthquakes from 1978 and 1980, for two of which similar non-DC mechanisms were determined, lie to the south, outside the area of the map.

erly orientation of the T axes for earthquakes near Casa Diablo Hot Springs than for earthquakes further east.

5.2. Source types

Fig. 6 shows our results on a ‘source-type plot’ (Hudson et al., 1989), which displays those characteristics of focal mechanisms that are independent of source orientation and scalar moment. In other words, the position of a mechanism on the plot depends only on the ratios of the principal moments. The horizontal coordinate is:

$$T \stackrel{\text{def}}{=} \frac{2m'_1}{|m'_3|} \quad (2)$$

which describes the type of shear deformation in-

volved (the relative sizes of the DC and CLVD components), and the vertical coordinate is:

$$k \stackrel{\text{def}}{=} \frac{m^{(v)}}{|m^{(v)}| + |m'_3|} \quad (3)$$

which measures the volume change. Here m'_1 and m'_3 are the absolutely smallest and largest deviatoric principal moments and $m^{(v)} \stackrel{\text{def}}{=} (M_{xx} + M_{yy} + M_{zz})/3$ is the isotropic (volumetric) moment. The source-type plot has the property that, if the principal moments were statistically independent and uniformly distributed in some interval symmetric about zero, then equal areas on the plot would have equal probabilities. Both T and k range from -1 to $+1$. A mechanism with an axis of rotational symmetry, such as a dipole, idealized tensile crack, or pure CLVD, has $T = +1$

if the dominant dipole is directed inward and $T = -1$ if it is directed outward. For deviatoric (no volume change) sources, $k = 0$, whereas $k = +1$ for a perfectly isotropic explosion and $k = -1$ for an isotropic implosion. We use the parameters k and T to describe source types, instead of decomposing the mechanism into isotropic, DC, and CLVD components, because such decompositions are not unique and there is great confusion in the literature between various decomposition methods, some of which have pathological properties (Julian et al., 1998, fig. 2).

Most of the earthquake mechanisms obtained in this study involve volume increases; 21 out of 26 of the source types lie in the upper half of the plot of Fig. 6. The predominance of volume increases probably indicates that most earthquakes in this area occur in regions of high fluid pressure, and involve the opening of tensile cracks. Only a

few earthquakes involve decreases in volume, and the effect is small (k is close to zero). If these volume decreases are significant, the earthquakes must involve the closing of cracks or other voids, and probably indicate fluid pressures lower than the most compressive principal stress. Variation of fluid pressure in space and time is an expected consequence of fluid migration, of which the earthquakes are probably a direct manifestation.

Mechanisms near the DC point in the center of the source-type plot are consistent with simple shear faulting, while the others (the majority) probably involve a combination of shear and tensile faulting. Combined shear and tensile failure occurs on a small scale in the laboratory (Brace and Bombalakis, 1963) and evidence of it is seen in exhumed hydrothermal mineral deposits (Sibson, 1981). Such mixed-mode failure is an expected consequence of stress-field heterogeneity

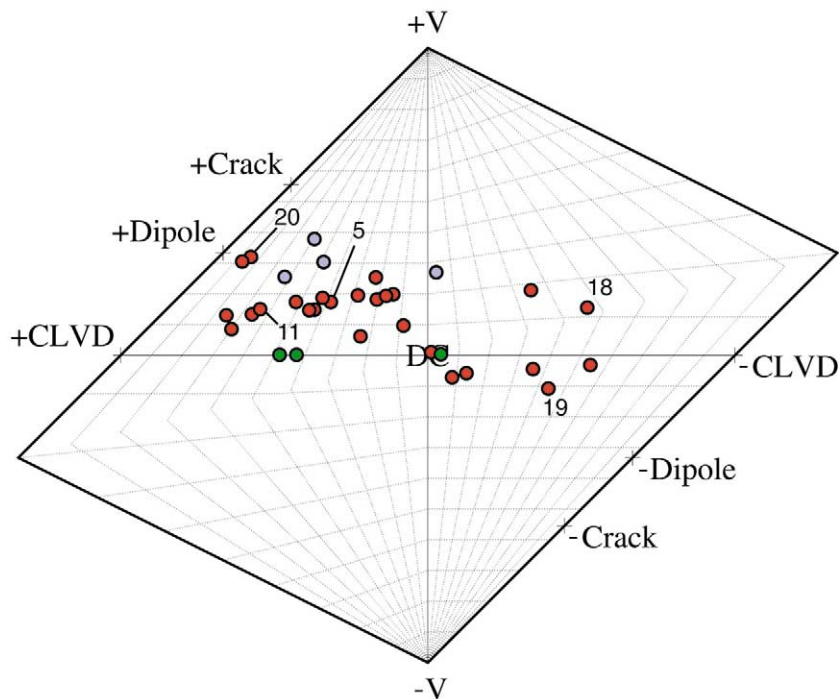


Fig. 6. Source-type plot (Hudson et al., 1989) of earthquake mechanisms shown in Fig. 5. Dotted lines: contours of constant k (Eq. 3), a measure of volume change, running from left to right, and constant T (Eq. 2), describing the deviatoric moment release, running from top to bottom. DC: double couple; \pm Crack: opening/closing tensile cracks; \pm Dipole: force dipoles directed outward/inward; \pm CLVD: compensated linear-vector dipoles with dominant dipoles directed outward/inward. Earthquake mechanisms are color-coded as in Fig. 5.

near the edges of faults and cracks. Stick-slip instability on auxiliary shear faults might also cause cracks to close suddenly and radiate seismic waves. Other mechanisms, involving material heterogeneity or special geometrical situations, can cause tensile cracks to open suddenly (Sammis and Julian, 1987), but these mechanisms would not apply to closing cracks.

The earthquake mechanisms at Long Valley caldera cannot, however, be explained completely by combinations of shear and tensile faulting. All such combinations must lie above and to the right of a line connecting the DC and +Crack points on the source-type plot, with the most plausible geometries lying close to this line (Julian et al., 1998). Most of the mechanisms of the earthquakes from Long Valley, on the other hand, lie below and to the left of this line (approximately between the +Dipole and DC points, although a dipole equivalent force system corresponds to no obvious physical process). If simultaneous shear faulting and tensile cracking causes these earthquakes, as we suggest, then the observed source types also require some volume-compensating process, probably involving fluid flow, that reduces the magnitudes of their explosive components. Foulger and Long (1984) suggested that fluid might flow into tensile cracks in response to the pressure drop caused by crack opening. Such a process might account for the observed k values being systematically smaller than expected for tensile/shear crack combinations. This effect would vary with the compressibility of the fluid involved, with highly compressible fluids such as steam giving smaller compensating effects than less compressible fluids such as liquid water or magma.

The available data do not indicate any large difference between the source processes of large and small earthquakes. The source types of four M_w 4.5–4.9 earthquakes of November 1997 analyzed by Dreger et al. (2000), and three $M_w \sim 6$ earthquakes of May 1980 analyzed by Julian and Sipkin (1985) are shown alongside those we report here in Figs. 5 and 6. The source orientations and (except for the fact that the 1980 mechanisms were constrained to lie on the line $k=0$) the source types are similar, which suggests that the

larger earthquakes and the microearthquakes we have analyzed are genetically similar. The four mechanisms reported by Dreger et al. (2000) have volume increases that are as large as the largest we observe here, but these results are not adequate to firmly establish a significant correlation of source type with earthquake size or time.

5.3. 'Spasmodic-burst' earthquakes

Two of the earthquakes reported here, events 20 and 21, occurred under the southwest flank of Mammoth Mountain about 33 s apart as part of a 'spasmodic burst' (Hill et al., 1990). These rapid-fire earthquake sequences have been common in Long Valley caldera and at Mammoth Mountain since the late 1970s. The mechanisms of earthquakes 20 and 21 are similar, and they have the most extreme source types of the events we analyzed, with both the largest k values (large volume increases) and most negative T values (indicating approximate rotational symmetry about their T axes). These characteristics suggest that the source processes are dominated by nearly pure mode I faulting (crack opening), with little or no shear faulting. The hypocentral locations of earthquakes 20 and 21 lie close to a NW-striking vertical plane normal to their T axes, which is the expected orientation of a mode I crack.

Although these spasmodic-burst earthquakes have the largest k values of the events studied here, these values are still significantly lower than those for pure tensile faulting, and require a volume-compensating process, such as rapid fluid flow. The required effect is small, however, and this fact may, as discussed above, indicate a highly mobile compensating fluid, such as steam or CO_2 . Three of the earthquakes of November 1997 studied by Dreger et al. (2000) have source types similar to those of the spasmodic-burst earthquakes, which suggests that their source processes may be similar.

5.4. Earthquakes at Mammoth Mountain

Earthquake mechanisms beneath Mammoth Mountain are more diverse than those in the south moat, in both their source types and their

source orientations. Events 20 and 21, discussed above, lie to the extreme left side of the source-type plot, and are consistent with partially compensated, nearly pure tensile failure, with insignificant shear faulting. Two other events (25, 26) lie in the otherwise sparsely populated right half of the source-type plot. The significance of these source types is not clear. Despite their close proximity to one another, the earthquakes beneath Mammoth Mountain have source orientations that are much more variable than those of events elsewhere. Five of these, events 19, 20, 21, 22, and 23, have subhorizontal T axes that trend approximately toward the summit of the mountain, suggesting that the volcano, because of either its weight or active processes within it, significantly affects the local stress field.

5.5. Earthquakes within the caldera

The focal-sphere coverage that the 1997 temporary network provided is best for earthquakes in the south moat west of Casa Diablo Hot Springs. One earthquake in this region (event 2) has a mechanism close to a DC, but most have source types with k values in the range from +0.15 to +0.26 and T values ranging down to -0.77 , consistent with a combination of tensile and shear faulting and a volume-compensating process. Most of the earthquakes have similar source orientations, with subhorizontal T axes trending northeast to north-northeast.

One group of a few hundred earthquakes in the caldera, east of the south moat and just south-southeast of the edge of the resurgent dome, lie

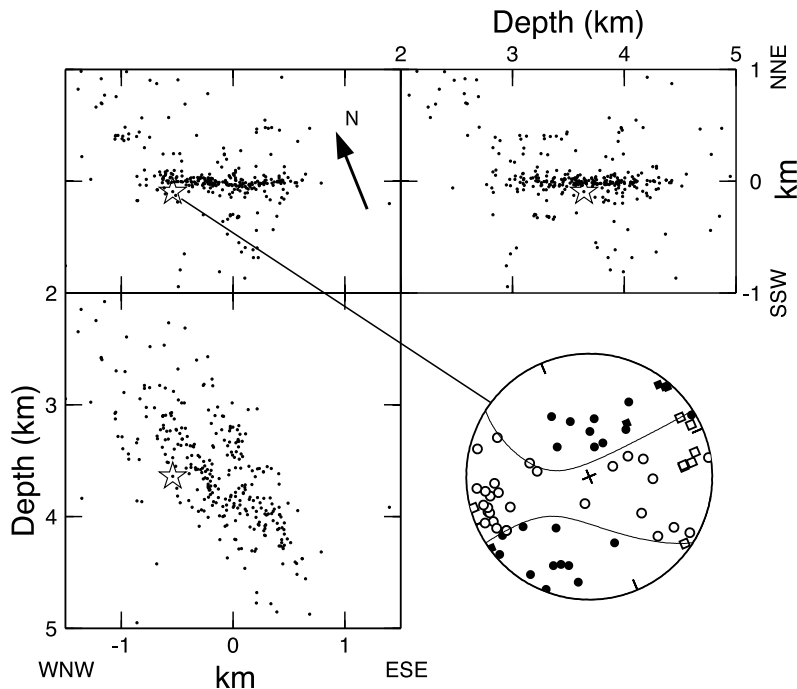


Fig. 7. Non-shear fault plane delineated by microearthquake hypocenters. Views from three orthogonal directions showing the locations of the 314 earthquakes (black dots) within the oblique rectangle shown in Fig. 1 that lie between 2 and 5 km depth. Upper left: map view; upper right: SSW–NNE vertical cross-section (viewing direction: 292°); lower left: WNW–ESE vertical cross-section (viewing direction: 22°). Star: earthquake 11 (see Tables 1 and 2 and Fig. 4f). Lower right: mechanism of earthquake 11, shown as an upper-hemisphere plot of P -wave polarities and our derived nodal curves. Data symbols are the same as those of Fig. 4. The focal sphere is rotated in the same way as the map at upper right, so that the fault plane defined by the seismicity is horizontal on the figure. The mechanism for this earthquake is incompatible with shear faulting on this plane, but is compatible with compensated tensile failure on this plane.

in a well-resolved failure zone whose orientation, along with the observed *P*-wave polarities, indicates that they cannot be caused by simple shear faulting. This evidence is independent of that provided by seismic-wave amplitude ratios, and thus is not subject to any errors to which those data might be prone. These earthquakes, which include events 9, 10, and 11, occurred from 15 July to 1 August and their hypocenters clearly define a vertical plane about 1.5 km long striking ESE at about 112° (Figs. 1 and 7). Most of the earthquakes in this cluster occurred on 17 and 18 July. After that, seismicity in this area fell to a low level and remained low until 12–14 November, when vigorous earthquake swarm activity resumed and propagated rapidly toward the west-northwest by about 3 km along an extension of the plane defined in July. This seismicity plane bisects the dilatational fields of the focal spheres of the events (Fig. 4e) and has just the orientation expected for a tensile crack corresponding to this source mechanism (normal to the *T* axis). The orientation of the plane is completely incompatible with shear-fault interpretations of the DC components of the focal mechanisms of these earthquakes, which require planes striking at 69° or 156°. This type of joint interpretation of earthquake focal mechanisms and high-resolution relative earthquake locations is a potentially powerful method for elucidating the physics of the earthquake process.

6. Interpretation and discussion

6.1. Comparison with previous results from Long Valley caldera

The earthquakes described here are the smallest at Long Valley caldera for which non-DC mechanisms have been reported, and the fact that they occur places constraints on the physical processes involved. The non-DC earthquakes of October 1978 and May 1980 had $M_w \sim 6$ (Julian, 1983; Julian and Sipkin, 1985) and those of November 1997 M_w 4.6–4.9 (Dreger et al., 2000). These large earthquakes all had substantial CLVD components, and the opening of cracks with volumes

of 6.4×10^4 to 7×10^4 m³, accompanied by compensating flow of magmatic or geothermal fluids, was suggested as possible sources. If the small non-DC earthquakes reported here are interpreted in the same way, the volumes of the intruded material range from about 0.06 to 600 m³. For a crack with an aspect ratio of about 10⁴ (see Dreger et al., 2000; Julian and Sipkin, 1985), these volumes correspond to cracks 4–85 m long and 0.4–8.5 cm thick. Such thin cracks are unlikely to be magmatic dikes. Furthermore, the hypocenters of the earthquakes beneath Casa Diablo Hot Springs that we studied lie between 2.9 and 6.1 km b.s.l. Deformation modeling suggests that the source of inflation beneath Casa Diablo Hot Springs is about 11 km b.s.l. (Langbein et al., 1995), so it is unlikely that magma is present at depths of 3–6 km. It has been suggested on the basis of seismic attenuation measurements that magma extends up to 2 km b.s.l. beneath Casa Diablo Hot Springs (Sanders, 1984; Sanders and Ryall, 1983). However, we find no evidence for such magma in local earthquake *P*- and *S*-wave speed tomography (Foulger et al., 2002). These facts suggest that the small, non-DC earthquakes we analyze beneath the Casa Diablo Hot Springs area do not result from magma intrusion.

The same reasoning may be applied to the earthquakes beneath Mammoth Mountain that we studied. These earthquakes ranged in magnitude from 0.78 to 1.55. Their mechanisms had both positive and negative CLVD components (*T* values) and they occurred from –0.4 to 2.8 km b.s.l. The occurrence of long-period earthquakes southwest of Mammoth Mountain suggests that magma is present there between 7 and 20 km depth. Seismic and deformation data from 1989 suggest that a dike about 13 cm thick opened between –1 and 9 km b.s.l. beneath Mammoth Mountain (Langbein et al., 1993). The upper ~4 km may have been intruded with high-pressure water or gas rather than magma (Foulger et al., 2002). The earthquakes we studied occurred when seismic activity beneath Mammoth Mountain was at a background level, notwithstanding the vigorous swarm occurring simultaneously in the south moat. It is unlikely that background seismic activity beneath Mammoth

Mountain results from continuous injection of very small magmatic dikes on a daily basis.

This reasoning raises the question of whether the same processes are responsible for both the larger non-DC earthquakes of 1978, 1980, and November 1997 and the small earthquakes we analyze. Earthquakes caused by simultaneous shear and tensile faulting have mechanisms that fall within a triangle lying to the right of the line connecting the DC and +Crack points on a source-type plot (Fig. 8a) (Julian et al., 1998). Mechanisms such as ours that lie to the left of this line might be caused by such mixed-mode faulting accompanied by a process that reduces the volume change, such as rapid inflow of fluid, as discussed above. Such a process has been suggested to explain similar mechanisms at The Geysers geothermal field (Ross et al., 1999). Mammoth Mountain has been degassing CO₂ at a rate of up to 500 tons/day since 1989 (Farrar et al., 1995) and evidence of changes in compressional- and shear-wave speeds inferred from repeat seismic tomography suggests that significant redistribution of gas occurred in the volcano edifice between 1989 and 1997 (Foulger et al., 2002). Migrating CO₂ and high-temperature steam and water may thus influence the focal mechanisms we observe beneath Mammoth Mountain. The mechanisms that have large –CLVD components may represent cavities that become underpressurized and collapse, ejecting their fluid.

In the case of earthquakes as large as $M_w \sim 6$, which are inferred to have been caused by the injection of up to $\sim 7 \times 10^8$ m³ of material into opening cracks, estimates of magma viscosities cannot absolutely rule out magmatic dike injection (e.g. Julian and Sipkin, 1985). If some earthquakes are generated by rapid magma injection, which may only generate large earthquakes, a surfeit of large-magnitude earthquakes might be expected, and indeed the occurrence of four $M_w \sim 6$ earthquakes within two days in May 1980 was very unusual. Also, the four non-DC earthquakes that occurred on or after 22 November 1997 (Dreger et al., 2000) accompanied a significant decrease in *b*-value (slope of the earthquake log-(frequency)–magnitude distribution curve) from 1.25 to 0.9, indicating an increase in the propor-

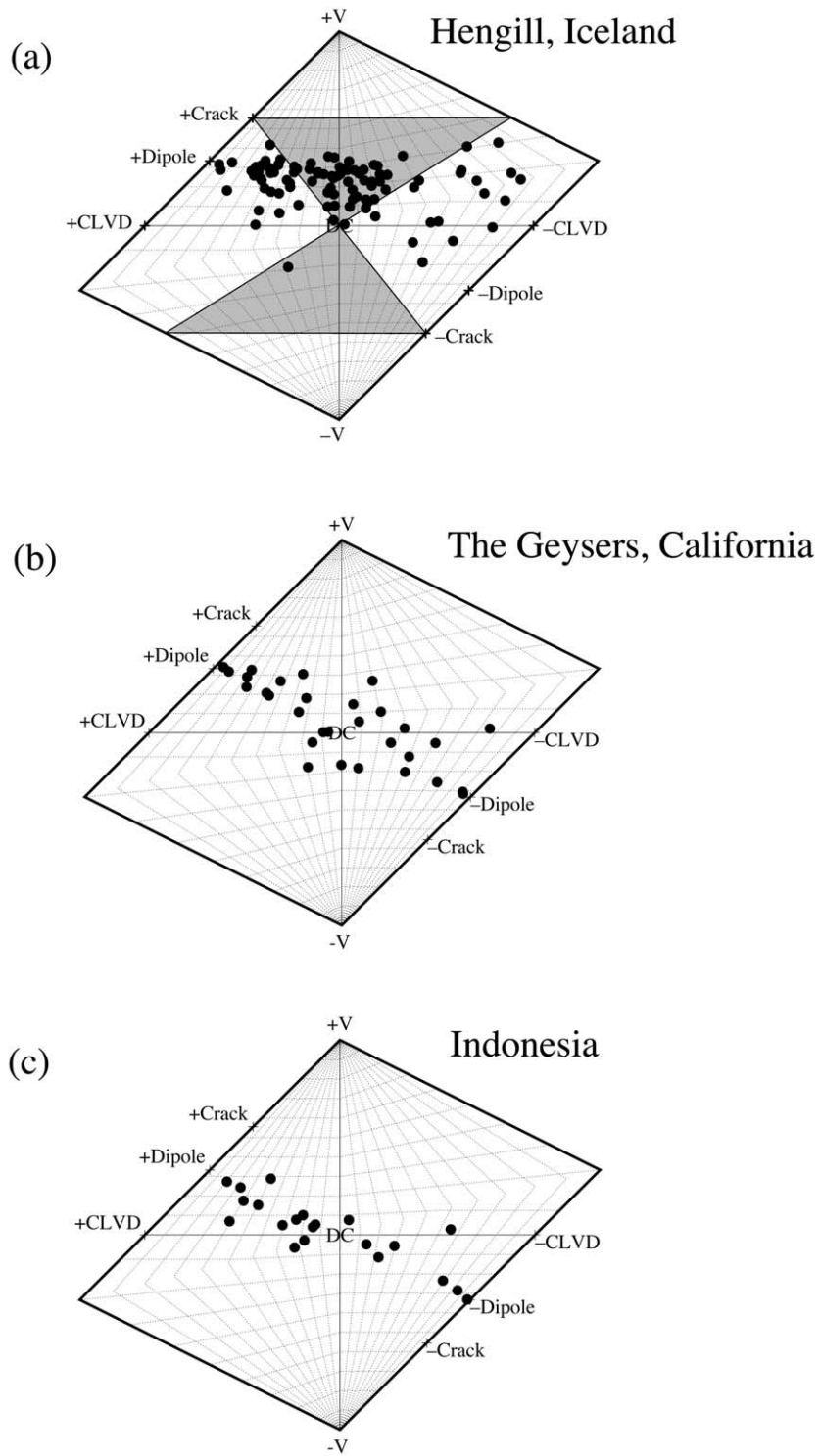
tion of large earthquakes (Barton et al., 1999). Both Julian and Sipkin (1985) and Dreger et al. (2000) report source durations an order of magnitude greater than typical for the non-DC earthquakes they studied, an effect that is expected if fluid motion plays a major role in the source process. Unfortunately, this process is not well enough understood to be able to infer the viscosity or other properties of the fluid involved, or to distinguish between magmatic or hydrothermal fluids.

6.2. Comparison with other volcanic and geothermal areas

Microearthquake source-mechanism studies similar to this one have been conducted at The Geysers geothermal area, California (Ross et al., 1996, 1999), the Hengill geothermal area, in southwestern Iceland (Miller et al., 1998b), and an exploited geothermal area in Indonesia (Fig. 8). Like the Casa Diablo Hot Springs area, The Geysers and the Indonesian area are commercially exploited, although on a larger scale. At The Geysers and the Indonesian field, many of the earthquakes are probably induced by volumetric collapse caused by decreases in pore pressure in the reservoirs.

Source types for earthquakes from The Geysers and the Indonesian field lie close to the line connecting the +Dipole and –Dipole points (Ross et al., 1999) (Fig. 8b,c). With one exception, the earthquakes from the Casa Diablo Hot Springs area all lie near the upper half of this line, between the +Dipole and DC points and earthquakes with negative CLVD and implosive volumetric ($T > 0$, $k < 0$) components seen elsewhere are rare or absent. The absence of such source types suggests that, unlike exploited geothermal fields undergoing volumetric contraction, most of the seismogenic volume beneath Casa Diablo Hot Springs is expanding. Near the Casa Diablo Hot Springs power plant, contraction is occurring locally (Sorey et al., 1995), and this is the location of one of the few implosive earthquakes (event 6) we found.

The distribution in source-type space of the Long Valley caldera earthquakes resembles most



closely that of the Hengill-Grensdalur area, Iceland (Miller et al., 1998b) (Fig. 8a). The volumetric components are essentially all zero or positive, within the expected errors, and the CLVD components are mostly positive ($T < 0$). The Hengill-Grensdalur volcanic complex lies in the extensional accretionary plate boundary in Iceland, and contains a large geothermal field that is unexploited except for a small, distal, part. Almost all of the 70 earthquakes from that area studied by Miller et al. (1998b) [#1248] have zero or positive volumetric components, the only exception being a single earthquake with an implosive component from the exploited area. The T values vary from -0.9 to $+0.8$.

The volumetric components of earthquakes from all the areas studied to date are restricted, with k values in the range $-0.3 \leq k \leq 0.3$. No earthquakes have yet been reliably observed that have explosive or implosive components as large as pure opening or closing cracks, which have $k = \pm 0.556$ (Figs. 6 and 8). Instead, the k values appear to have limits close to the values for dipole sources ($k = \pm 1/3$). Opening cracks that are only partially compensated by fluid flow might coincidentally have moment tensors equivalent to dipoles. However, the reason for this apparent limitation in natural seismic sources in the Earth is not yet well understood.

7. Conclusions

1. Most of the small ($0.4 < M_w < 3.1$) earthquakes that occurred in the summer and early fall of 1997 during a time of accelerating earthquake swarms and inflationary crustal deformation at Long Valley caldera have non-DC mechanisms with positive CLVD and isotropic (volume increase) components.
2. The source types of most of these earthquakes are consistent with mixed shear and tensile

faulting, but require an additional volume-compensating process, which might be provided by the flow of fluid into opening tensile cracks.

3. A cluster of a few hundred earthquakes at the east end of the south moat of the caldera clearly defines a vertical fault plane striking at 112° . Their focal mechanisms have T axes normal to this plane, and therefore rule out shear faulting as the source process, but are compatible with the fault being a tensile crack.
4. Two earthquakes from a ‘spasmodic burst’ at Mammoth Mountain have nearly identical focal mechanisms, which are close to pure dipoles and are consistent with compensated tensile faulting. The degree of volumetric compensation is low, possibly reflecting low mobility or high compressibility of the acting fluid. These are the first focal mechanisms determined for spasmodic burst earthquakes.
5. Earthquake source orientations at Mammoth Mountain vary systematically about the edifice, and suggest that the volcano plays a significant role in controlling the orientation of the local stress field.
6. Comparison with earthquake mechanisms from other areas suggests that extensional areas such as Long Valley caldera are characterized by non-DC mechanisms involving volume increases and having positive CLVD components. Earthquakes with volume decreases are common only in exploited geothermal areas.

Acknowledgements

The instruments used in the field program were provided by the Natural Environment Research Council (NERC loan 540/0197) and the PASS-CAL facility of the Incorporated Research Institutions for Seismology (IRIS) through the Stan-

Fig. 8. Source-type plots of earthquake mechanisms from (a) the Hengill-Grensdalur volcanic complex, Iceland (after Miller et al., 1998b), (b) The Geysers geothermal area, California (after Ross et al., 1999), and (c) a commercially exploited geothermal area in Indonesia. “Triangles in (a) indicate loci of combined shear and tensile faulting with all possible orientations and relative moments.” Compare with Fig. 6.

ford Instrument Center. Data collected during this experiment will be available through the IRIS Data Management Center. The facilities of the IRIS Consortium are supported by the National Science Foundation under Cooperative Agreement EAR-9023502. We thank the U.S. Forest Service for permission to deploy seismic stations and for assistance, and Dan Lister of the Mono County Government for invaluable practical help. The California Institute of Technology contributed two broadband seismometers with 24-bit data loggers and auxiliary equipment. A. Strujkova, D. Schleupner, P. Boyd, R. Perlröth, L.E. Foulger, N. Dotson, G. Sharer, E. Brodsky, M. Alvarez and A. Newman contributed to the fieldwork. We thank Paul Davis of UCLA for kindly lending a 24-bit REFTEK data logger on short notice during the 1997 field experiment. The manuscript was improved by valuable reviews by Arthur McGarr and David Oppenheimer.

References

- Anderson, D.L., Archambeau, C.B., 1964. The anelasticity of the Earth. *J. Geophys. Res.* 69, 2071–2084.
- Arnott, S.K., Foulger, G.R., 1994. The Krafla spreading segment, Iceland: 2. The accretionary stress cycle and non-shear earthquake focal mechanisms. *J. Geophys. Res.* 99, 23827–23842.
- Bailey, R.A., Dalrymple, G.B., Lanphere, M.A., 1976. Volcanism, structure, and geochronology of Long Valley Caldera, Mono County, California. *J. Geophys. Res.* 81, 725–744.
- Barker, J.S., Langston, C.A., 1983. A teleseismic body wave analysis of the May, 1980 Mammoth Lakes, California earthquakes. *Bull. Seismol. Soc. Am.* 73, 419–434.
- Barton, D.J., Foulger, G.R., Henderson, J.R., Julian, B.R., 1999. Frequency-magnitude statistics and spatial correlation dimensions of earthquakes at Long Valley caldera, California. *Geophys. J. Int.* 138, 563–570.
- Brace, W.F., Bombalakis, E.G., 1963. A note on brittle crack growth in compression. *J. Geophys. Res.* 68, 3907–3913.
- Claerbout, J.F., Muir, F., 1973. Robust modeling with erratic data. *Geophysics* 38, 826–844.
- Console, R., Rosini, R., 1998. Non-double-couple microearthquakes in the geothermal field of Larderello, central Italy. *Tectonophysics* 289, 203–220.
- Denlinger, R.P., Riley, F.S., Boling, J.K., Carpenter, M.C., 1985. Deformation of Long Valley caldera between August 1982 and August 1983. *J. Geophys. Res.* 90, 11199–11209.
- Dreger, D.S., Tkalčić, H., Johnston, M., 2000. Dilational processes accompanying earthquakes in the Long Valley caldera. *Science* 288, 122–125.
- Ekström, G., Dziewonski, A.M., 1983. Moment tensor solutions of Mammoth Lakes earthquakes. *EOS Trans. AGU* 64, 262.
- Farrar, C.D. et al., 1995. Forest-killing diffuse CO₂ emission at Mammoth Mountain as a sign of magmatic unrest. *Nature* 376, 675–678.
- Foulger, G.R., 1988. Hengill triple junction, SW Iceland; 2. Anomalous earthquake focal mechanisms and implications for process within the geothermal reservoir and at accretionary plate boundaries. *J. Geophys. Res.* 93, 13507–13523.
- Foulger, G.R., Julian, B.R., 1993. Non-double-couple earthquakes at the Hengill-Grensdalur volcanic complex, Iceland: Are they artifacts of crustal heterogeneity? *Bull. Seismol. Soc. Am.* 83, 38–52.
- Foulger, G.R. et al., 2002. Three-dimensional crustal structure of Long Valley caldera, California, and evidence for the migration of CO₂ under Mammoth Mountain. *J. Geophys. Res.* 108, 2147, doi: 10.1029/2000JB0041.
- Foulger, G.R., Long, R.E., 1984. Anomalous focal mechanisms; tensile crack formation on an accreting plate boundary. *Nature* 310, 43–45.
- Foulger, G.R., Long, R.E., Einarsson, P., Björnsson, A., 1989. Implosive earthquakes at the active accretionary plate boundary in northern Iceland. *Nature* 337, 640–642.
- Foulger, G.R., Malin, P.E., Shalev, E., Julian, B.R., Hill, D.P., 1998. Seismic monitoring and activity increase in California caldera. *EOS Trans. AGU* 79, 357–363.
- Fuchs, K., Müller, G., 1971. Computation of synthetic seismograms with the reflectivity method and comparison with observations. *Geophys. J. R. Astron. Sci.* 23, 417–433.
- Hill, D.P., 1996. Earthquakes and carbon dioxide beneath Mammoth Mountain, California. *Seismol. Res. Lett.* 67, 8–15.
- Hill, D.P., Bailey, R.A., Ryall, A.S., 1985. Active tectonic and magmatic processes beneath Long Valley caldera, eastern California: An overview. *J. Geophys. Res.* 90, 11111–11120.
- Hill, D.P. et al., 1990. The 1989 earthquake swarm beneath Mammoth Mountain, California: An initial look at the 4 May through 30 September activity. *Bull. Seismol. Soc. Am.* 80, 325–339.
- Hudson, J.A., Pearce, R.G., Rogers, R.M., 1989. Source type plot for inversion of the moment tensor. *J. Geophys. Res.* 94, 765–774.
- Hung, S.-H., Forsyth, D.W., 1996. Non-double-couple focal mechanisms in an oceanic, intraplate earthquake swarm: Application of an improved method for comparative event, moment tensor determination. *J. Geophys. Res.* 101, 25347–25371.
- Julian, B.R., 1983. Evidence for dyke intrusion earthquake mechanisms near Long Valley caldera, California. *Nature* 303, 323–325.
- Julian, B.R., 1986. Analysing seismic-source mechanisms by linear-programming methods. *Geophys. J. R. Astron. Sci.* 84, 431–443.

- Julian, B.R., 1994. Volcanic tremor: Nonlinear excitation by fluid flow. *J. Geophys. Res.* 99, 11859–11877.
- Julian, B.R., Foulger, G.R., 1996. Earthquake mechanisms from linear-programming inversion of seismic-wave amplitude ratios. *Bull. Seismol. Soc. Am.* 86, 972–980.
- Julian, B.R., Miller, A.D., Foulger, G.R., 1998. Non-double-couple earthquakes I: Theory. *Rev. Geophys.* 36, 525–549.
- Julian, B.R., Sipkin, S.A., 1985. Earthquake processes in the Long Valley caldera area, California. *J. Geophys. Res.* 90, 11155–11169.
- Knopoff, L., Randall, M.J., 1970. The compensated linear vector dipole: A possible mechanism for deep earthquakes. *J. Geophys. Res.* 75, 4957–4963.
- Kubas, A., Sipkin, S.A., 1987. Non-double-couple earthquake mechanisms in the Nazca Plate subduction zone. *Geophys. Res. Lett.* 14, 339–342.
- Langbein, J., 1989. The deformation of the Long Valley caldera, eastern California, from mid-1983 to mid-1988; measurements using a two-color geodimeter. *J. Geophys. Res.* 94, 3833–3850.
- Langbein, J., Hill, D.P., Parker, T.N., Wilkinson, S.K., 1993. An episode of reinflation of the Long Valley Caldera, Eastern California: 1989–1991. *J. Geophys. Res.* 98, 15851–15870.
- Langbein, J.D., Dzurizin, D., Marshall, G., Stein, R., Rundle, J., 1995. Shallow and peripheral volcanic sources of inflation revealed by modeling two-color geodimeter and leveling data from Long Valley caldera, California, 1988–1992. *J. Geophys. Res.* 100, 12487–12495.
- Miller, A.D., 1996. Seismic Structure and Earthquake Focal Mechanisms of the Hengill Volcanic Complex, SW Iceland. Ph.D. Thesis, University of Durham, Durham, 280 pp.
- Miller, A.D., Foulger, G.R., Julian, B.R., 1998a. Non-double-couple earthquakes. II: Observations. *Rev. Geophys.* 36, 551–568.
- Miller, A.D., Julian, B.R., Foulger, G.R., 1998b. Three-dimensional seismic structure and moment tensors of non-double-couple earthquakes at the Hengill-Grensdalur volcanic complex, Iceland. *Geophys. J. Int.* 133, 309–325.
- Pitt, A.M., Hill, D.P., 1994. Long-period earthquakes in the Long Valley caldera region, eastern California. *Geophys. Res. Lett.* 21, 1679–1682.
- Prejean, S.G., Ellsworth, W.L., 2001. Observations of earthquake source parameters and attenuation at 2 km depth in the Long Valley Caldera, eastern California. *Bull. Seismol. Soc. Am.* 91, 165–177.
- Ross, A., Foulger, G.R., Julian, B.R., 1996. Non-double-couple earthquake mechanisms at The Geysers geothermal area, California. *Geophys. Res. Lett.* 23, 877–880.
- Ross, A., Foulger, G.R., Julian, B.R., 1999. Source processes of industrially-induced earthquakes at The Geysers geothermal area, California. *Geophysics* 64, 1877–1889.
- Rundle, J.B., Hill, D.P., 1988. The geophysics of a restless caldera – Long Valley, California. *Annu. Rev. Earth Planet. Sci.* 16, 251–271.
- Sammis, C.G., Julian, B.R., 1987. Fracture instabilities accompanying dike intrusion. *J. Geophys. Res.* 92, 2597–2605.
- Sanders, C.O., 1984. Location and configuration of magma bodies beneath Long Valley, California, determined from anomalous earthquake signals. *J. Geophys. Res.* 89, 8287–8302.
- Sanders, C.O., Ryall, F., 1983. Geometry of magma bodies beneath Long Valley, California, determined from anomalous earthquake signals. *Geophys. Res. Lett.* 10, 690–692.
- Saraò, A., Panza, G.F., Privitera, E., Cocina, O., 2001. Non-double-couple mechanisms in the seismicity preceding the 1991–1993 Etna volcano eruption. *Geophys. J. Int.* 145, 319.
- Savage, J.C., Cockerham, R.S., 1984. Earthquake swarm in Long Valley caldera, California, January 1983: Evidence for dike inflation. *J. Geophys. Res.* 89, 8315–8324.
- Shimizu, H., Matsuwo, N., Ohmi, S., Umakoshi, K. and Urabe, T., 1988. A non double-couple seismic source: Tensile-shear crack formation in the Unzen volcanic region, *Seismol. Res. Lett.*, 5 pp.
- Sibson, R.H., 1981. Fluid flow accompanying faulting: Field evidence and models. In: *Earthquake Prediction – An International Review*. Maurice Ewing Series. AGU, Washington, DC, pp. 593–603.
- Sorey, M.L. et al., 1998. Carbon dioxide and helium emissions from a reservoir of magmatic gas beneath Mammoth Mountain, California. *J. Geophys. Res.* 103, 15303–15323.
- Sorey, M.L., Farrar, C.D., Marshall, G.A., Howle, J.F., 1995. Effects of geothermal development on deformation in the Long Valley caldera, eastern California, 1985–1994. *J. Geophys. Res.* 100, 12475–12486.
- Sorey, M.L., Kennedy, B.M., Evans, W.C., Farrar, C.D., Suemnicht, G.A., 1993. Helium isotope and gas discharge variations associated with crustal unrest in Long Valley caldera, California, 1989–1992. *J. Geophys. Res.* 98, 15871–15889.
- Stroujkova, A.F., Malin, P.E., 2000. A magma mass beneath Casa Diablo? Further evidence from reflected seismic waves. *Bull. Seismol. Soc. Am.* 90, 500–511.
- Vavrycuk, V., 2002. Non-double-couple earthquakes of 1997 January in west Bohemia, Czech Republic: Evidence of tensile faulting. *Geophys. J. Int.* 149, 364–373.
- Waldhauser, F., Ellsworth, W.L., 2000. A double-difference earthquake location algorithm: Method and application to the northern Hayward fault, California. *Bull. Seismol. Soc. Am.* 90, 1353–1368.